A Stationary Hemispherical SPECT Imager for Three-Dimensional Brain Imaging

Robert K. Rowe, John N. Aarsvold, Harrison H. Barrett, Jyh-Cheng Chen, William P. Klein, Bruce A. Moore, Irene W. Pang, Dennis D. Patton and Timothy A. White

Radiology Department, Arizona Health Sciences Center and the Optical Sciences Center, University of Arizona, Tucson, Arizona

A completely stationary, hemispherical-coded aperture SPECT imaging system was designed to produce three-dimensional images of the brain. The system consisted of a hemispherical multiple-pinhole coded aperture and 20 small (100 × 100 mm crystal area) digital gamma cameras. Reconstructions and measured performance specifications from two laboratory versions of the imager are presented. The reconstructed field of view of these systems was an ellipsoidal region with semi-diameters of 100 × 100 × 50 mm. The reconstructed spatial resolution for a point source in air at the center of this field was found to be 4.8 mm FWHM and the corresponding system sensitivity was 36 cps/μCi. An analysis using an ideal-observer model indicated that the multiplexed projection data suffered a 21% degradation relative to similar, but nonmultiplexed SPECT data. Therefore, by this measure, the effective sensitivity of the brain imager was 79% of the measured value.

J Nucl Med 1993; 34:474–480

Figure 1. The three-dimensional SPECT data are collected by placing the patient's head within a lead-alloy hemispherical shell which contains a large number of small pinholes. This array of pinholes will be referred to as the "aperture." Each of the pinholes allows a different projection of the activity distribution to pass through the aperture and onto the detector surface. These projections may overlap, resulting in multiplexing or coding of the projection data. The aperture that produces such projection data is referred to as a hemispherical multiple-pinhole coded aperture (MPCA). The detector surface is made up of modular cameras that are packed in a hemispherical pattern surrounding the aperture. A single set of pinhole projections, obtained without motion of the aperture or detectors, provides the necessary data to reconstruct three-dimensional activity distribution in the patient's brain.

METHODS

We began our investigation of the brain imager by performing a simulation study, which generated three-dimensional SPECT images from various hemispherical MPCA imagers of different system configurations. Based upon a comparison of the simulation results, we designed and built two laboratory versions of the imager, both of which had system geometries similar to the simulated system that produced the best reconstructions. We first constructed a partial imaging system capable of emulating a full imager with the assumption of system symmetry. We later built a complete, fully equipped prototype system. Both of these systems were used to image a number of different three-dimensional SPECT phantoms and to measure several important system performance characteristics.

The system parameters that were varied during the course of the simulation study were the ones that have the greatest effect on the performance of a modular camera MPCA system: the number, size and placement of the pinholes, and the number and placement of the modular cameras. In order to reduce the scope of our study to a manageable size, we chose to consider only hemispherical imaging geometries. The detector surface and the aperture were both hemispherical and concentric with the center of the field of view (FOV).

T he radiology research group at the University of Arizona had previously developed a modular scintillation camera and incorporated it in several unique SPECT systems (*1–4*). These modular scintillation cameras are small, digital gamma cameras with an active area of 10 × 10 cm. The spatial resolution (2.8 mm FWHM in the center of the field), energy resolution (10% at 140 keV) and count-rate capability (120 kcps) of each module are comparable to those of full-size, commercial scintillation cameras, but each module is mechanically, optically and electronically independent of the others. We have designed and built several different SPECT imaging systems based upon the modular cameras, including a stationary, multiple-slice cardiac imaging system (*5–7*) and a fully three-dimensional, stationary brain imager (*8–10*). It is this latter system that we describe in this article.

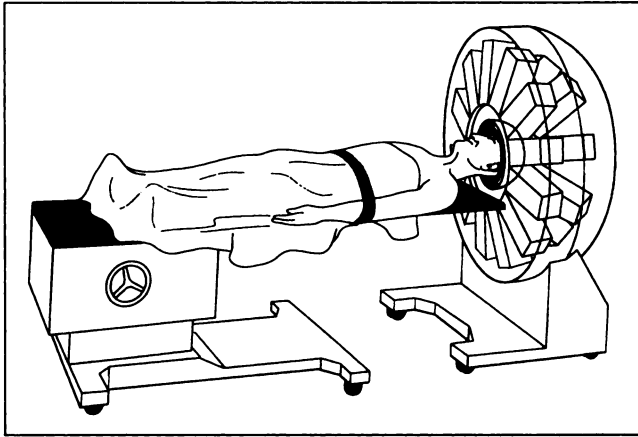An artist's conception of the brain imager is shown in

FIGURE 1. Conceptual sketch of the UA brain imager designed to perform three-dimensional SPECT imaging with no system motion. The imager consists of a lead-alloy hemispherical multiple-pinhole coded aperture and 20 modular gamma cameras.

Simulation Study of the Brain Imager

The imaging characteristics of the three-dimensional brain imager can be described by a linear-systems model of the following form:

$$g = Hf. \qquad \text{Eq. 1}$$

In this formulation, the object is modeled as N discrete volume elements (voxels) with activity levels given by the elements of the N-element vector f. The corresponding SPECT data set is assumed to consist of M discrete picture elements (pixels) with counts given by the elements of the M-element vector g. The system is modeled by the M × N-element H matrix, which represents the spatially variant response function of the system.

The simulation routine used a numerical model of the imaging system to generate independently the system matrix H and data vector g for each system configuration studied. Both sets of data included effects due to radiometry, photon noise, finite pinhole size, object attenuation and the spatial resolution of the detector. Scatter and detector energy resolution were not modeled by the simulation. The system matrix was produced by simulating a calibration procedure whereby a small point source was moved to each of the voxels within the FOV. The response of the imaging system to each of these source positions was recorded as a single column of the H matrix. The FOV used in all of the simulations was a 40 × 30 × 20 voxel region in which each voxel was a 5 mm cube.

The simulated data vector g was synthesized by a weighted sum of the projection data produced by each of the voxels contained in a three-dimensional digital phantom, where the weighting factor was proportional to the activity level of each voxel. A coarsely-sampled version of the digital brain phantom used during the simulation study is shown in Figure 2A. This version consists of 24,000 voxels, each a 5-mm cube, and is represented in the figure as 20 slices of 40 × 30 pixels. In order to better approximate a realistic, continuous object, the phantom that was actually used in the simulations was more finely sampled, consisting of 68 × 51 × 34 voxels with a voxel spacing
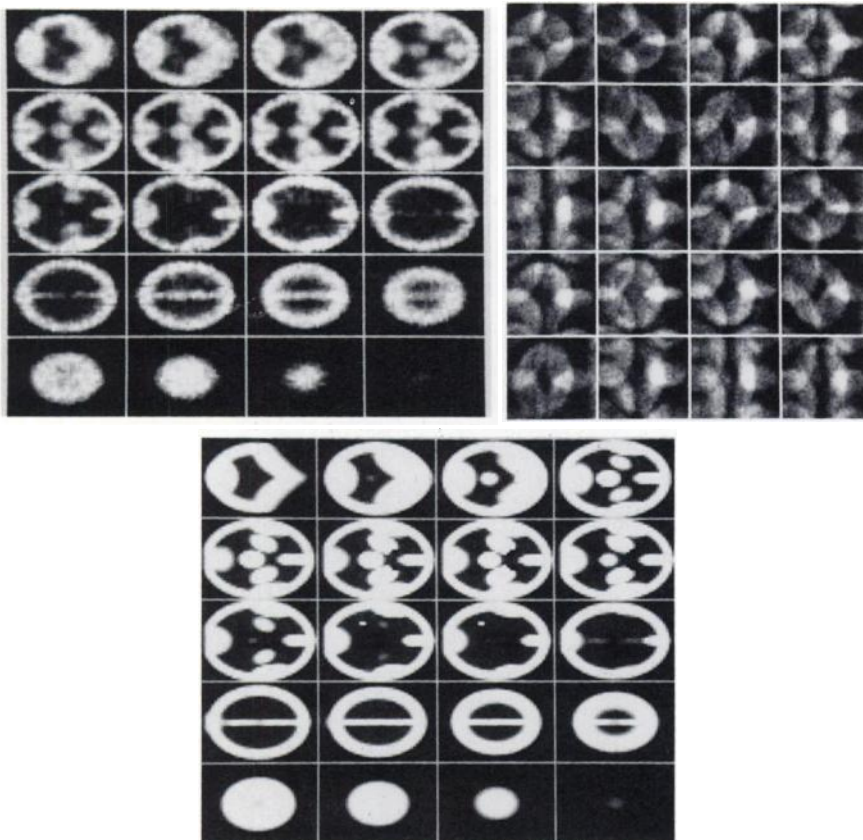

FIGURE 2. (A) Twenty slices through a digital brain phantom similar to the one used for the simulation studies. Each slice consists of 40 × 30 voxels, each 5 × 5 × 5 mm. The base of the brain phantom is shown in the upper left corner and consecutive slices are arranged in a raster pattern with the apex of the brain shown in the lower right corner of the image. (B) Projection data of the digital brain phantom as collected by the 20 modular cameras in a simulated imaging system similar to Figure 1. The aperture hemisphere had a radius of 15 cm and contained 100 pinholes, each 1.4 mm square. The cameras were arranged tangent to a 22-cm radius hemisphere. (C) Reconstruction of the digital brain phantom that was produced using the projection data described in (B). Both the projection data and the system matrix included effects due to photon noise and attenuation.

of 2.9 mm along each dimension. A typical set of projection data produced by this phantom is shown in Figure 2B. The simulated system that produced this data had 100 pinholes, each 1.4 mm^2, located on a hemisphere with a 15-cm radius and 20 cameras arranged tangent to a 22-cm radius hemisphere.

The modular cameras used in the simulation study differed somewhat from the cameras that were incorporated in the real systems. Both simulated and real cameras had a detector area of 100 × 100 mm. However, in order to easily approximate the actual spatial resolution of the real cameras and to increase the speed of the simulations, the simulated cameras divided the detector area into 32 × 32 pixels, each 3.1 mm^2, one-quarter of the 64 × 64 pixels used by the actual hardware.

An iterative search algorithm was used to reconstruct the original object vector f from the simulated system matrix H and projection data g (10). The reconstruction algorithm perturbed each voxel in the object estimate in such a way as to move the reconstruction toward the maximum likelihood estimate subject to a weighted smoothing constraint. This constraint was based upon the sum of the squared differences between the value of the voxel being perturbed and its nearest neighbors.

Figure 2C shows the reconstruction that resulted from the SPECT projection data shown in Figure 2B. The simulation assumed a total activity of 1 mCi within the digital brain phantom and an imaging time of 10 min. The H matrix was generated on a 5-mm voxel grid. The calibration source was assumed to be 6 mCi and imaged for 10 sec at each voxel location. The attenuating object was an ellipsoid approximating the size of a human brain with a constant linear attenuation coefficient of 0.15 cm^{-1}.

Brain Imager Laboratory Systems

Based upon a comparison of the reconstructions that resulted from a variety of simulated system configurations, we designed and built two laboratory versions of the brain imager. The initial version, a partial system containing a quarter of the full complement of cameras and pinholes, was capable of emulating a full imager using the assumption of fourfold symmetry of the system. This emulation system consisted of five modular gamma cameras with the detector surfaces tangent to a 22-cm radius hemisphere and a lead-alloy aperture with a 15-cm radius and 25 pinholes of 2 mm diameter. A complete set of projection data of an object was synthesized by using the emulation system to collect four views of the object with the object rotated a quarter turn between each collection period. Later, we constructed a full prototype imaging system. This system had the same geometry as the emulation system but was equipped with the full complement of 20 cameras and 100 pinholes. Images produced by both of these systems are shown and discussed in the following sections.

System Calibration

A robot was used to collect the H matrix for the imaging systems. The robot moved a small radioactive source to each of the calibration voxels in the object space and held the source stationary while the imager collected the projection data for a preset time. After the projection data were collected for all of the calibration voxels, a multiplicative correction was applied to the measured data to compensate for the radioactive decay of the source during the calibration process.

A common object space used by the three-dimensional brain imager consisted of 3.3 mm cubic voxels contained in an ellip-

soidal region with semi-diameters of 100 × 100 × 50 mm; such an object space contained approximately 74,000 cubic voxels. The 20 gamma cameras that viewed this object space yielded 81,920 detector measurements. Therefore, the H matrix for such a system had dimensions of 81,920 × 74,000, which was far too large to conveniently measure, store or process directly. Fortunately, the H matrices were relatively sparse—approximately 2% of the elements were non-zero after a moderate threshold was applied to the measured data—and therefore more efficient techniques could be used to collect and store the calibration data.

To reduce the measurement time and storage requirements of the system matrix, the H matrix was separated into two component matrices. One component, which we refer to as the R matrix, defined the total number of counts observed within the bounds of a particular pinhole projection and the location of the pinhole projection centroid as a function of the calibration source position. The second component, the B matrix or blur matrix, defined the two-dimensional profile of each of the pinhole projections as a function of the location of the projection centroid. With this technique, all of the geometric and radiometric information was contained in the R matrix, while the detector-specific information was contained in the B matrix.

The technique of separating the H matrix into two component matrices is well suited to use in conjunction with an interpolation scheme. The radiometric component, R, is a slowly varying function of the point-source location and thus can be interpolated to produce data corresponding to source positions between measured locations. The ability to interpolate these data allowed us to measure the system response function on a coarse, 10-mm grid and use the resulting data to generate an R matrix corresponding to a 3.3-mm grid. The B matrix is assumed to be a function of just the centroid location and independent of the point source location. Therefore, the B matrix could be generated directly from the coarse-grid H matrix. Using this separation technique, we could synthesize a 74,000-voxel fine-grid H matrix by measuring the system response at only 3,200 voxels, which typically took less than 10 hr.

Another advantage to separating the H matrix in the manner described is that the two component matrices are much smaller than the full H matrix. The application of simple data compression techniques allows both matrices to be stored in less than 80 megabytes of space. Moreover, portions of the component matrices can be recombined quickly and easily as needed during the reconstruction to generate only the necessary parts of the H matrix, thus omitting the necessity of ever storing or manipulating the entire H matrix at one time.

RESULTS

Three-Dimensional Phantom Reconstruction

One of the phantoms imaged with the emulation system is shown in Figure 3A. It consisted of a twisted, hollow acrylic tube with an inner diameter of 3 mm and two hollow spheres with inner diameters of 11.4 and 13.8 mm. The phantom had 1.7 mCi of ^{99m}Tc solution in the acrylic tube and approximately 0.6 mCi of solution in each of the hollow spheres. The tube and spheres were placed into an Alderson head phantom and the remaining volume was filled with water. Four different views of the phantom
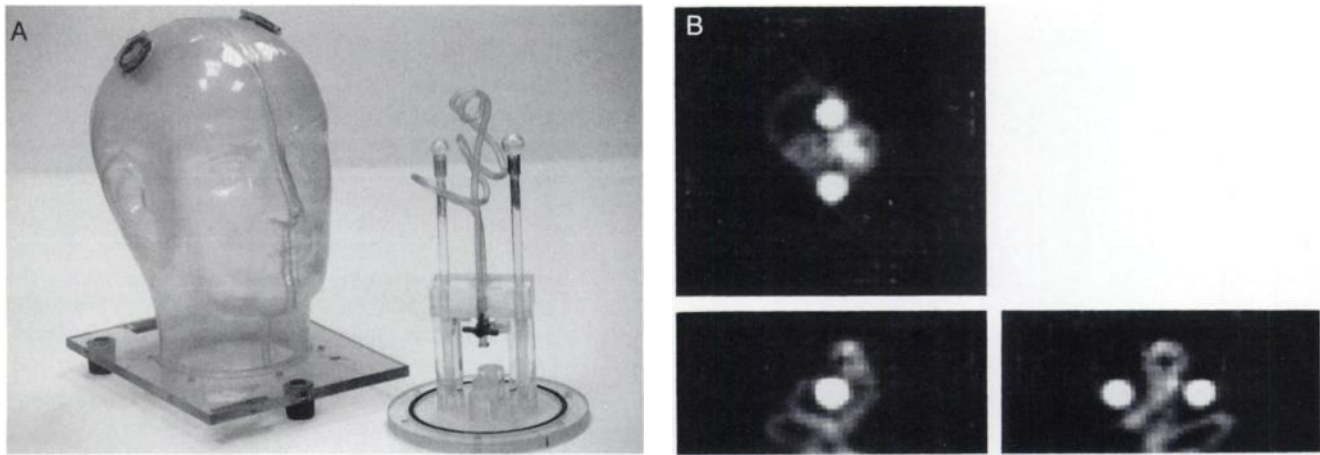
FIGURE 3. (A) Photograph of a three-dimensional phantom consisting of a hollow, twisted acrylic tube and two hollow spheres. The tube had an inner diameter of approximately 3.0 mm while the spheres had inner diameters of 11.4 and 13.8 mm. These components were filled with a ^{99m}Tc solution and placed inside the Alderson head phantom. The remaining volume of the head phantom was filled with water. (B) Reconstruction of the three-dimensional SPECT phantom shown in (A). The acrylic tube contained approximately 1.7 mCi of ^{99m}Tc, while the spheres contained approximately 0.6 mCi of ^{99m}Tc each. The phantom was imaged by the emulation system for 120 sec per view resulting in a projection data set that contained 4.2 million counts. This figure depicts the three-view orthographic projection of the three-dimensional reconstruction. The top view is shown in the upper left, the front is shown in the lower left and the right-side view is shown in the lower right.

were presented to the system by rotating the phantom 90° between data collection intervals. Each view was imaged for 120 sec, emulating a single 2-min collection interval on a full brain imaging system. The resulting projection data set contained 4.21 million counts.

The object space of the system was bounded by a 100 × 100 × 50 mm semi-diameter ellipsoid. The region within the ellipsoid was calibrated on a 10 × 10 × 10 mm grid and the resulting system response matrix was processed using the techniques just discussed to yield system response data on a 3.3-mm grid. These data were then corrected to model the object attenuation. The reconstruction was performed using the iterative search technique. Figure 3B shows the resulting three-dimensional reconstruction of the head phantom presented as a three-view orthographic projection.

Reconstructed Spatial Resolution

The reconstructed spatial resolution of the brain imager for a point source in air at the center of the FOV was measured using a 2-mm source that contained approximately 400 μCi of ^{99m}Tc and imaged for 120 sec. The same source was then used to directly measure a fine-grid system matrix with a voxel spacing of 2 mm. The calibrated region for this experiment was a 30 × 30 × 30 mm cube with the center of the cube approximately coincident with the center of the aperture hemisphere. Traces across the resulting reconstruction along any of the three axes of the voxel grid were nearly identical and had widths of approximately 5.2 mm FWHM. By assuming that the 2-mm source width was added in quadrature to the system resolution, we determined that the reconstructed spatial resolution of the system under these con-

ditions was 4.8 mm FWHM. The corresponding geometrical resolution, calculated from the simple pinhole imaging equation and including the 2.8 mm detector resolution, is approximately 8.7 mm FWHM. This suggests that some resolution is being recovered by the nonlinear reconstruction algorithm.

The reconstructed resolution of the imaging system was also demonstrated by using the prototype system to generate an image of a linear array of points. A SPECT data set was generated by moving a point source to nine different locations along a straight line and adding the projection data from each source location. The line was in the axial direction and passed through the center of the aperture hemisphere. The point source separation along the line was 10 mm center-to-center. The 2.5 mm point source contained approximately 8 mCi and was imaged for 10 sec at each of the nine positions along the array. The same point source was then used to directly measure the fine-grid H matrix on a 5 × 5 × 41 voxel grid with a grid spacing of 2.5 mm. The resulting three-dimensional reconstruction is shown in Figure 4A and a trace through the center of this image is shown in Figure 4B.

As a practical illustration of the system resolution, we produced several images of the familiar two-dimensional Hoffman brain phantom using the full system. A 10-min exposure with about 3 mCi in the phantom yielded 34 million counts. Figure 5 shows 12 slices through the three-dimensional reconstruction from this data set. In this figure, the reconstruction voxel size and the spacing between slices is 3.3 mm. The phantom is approximately 13 mm thick and occupies about four slices. The figure shows very little reconstructed activity outside this re-
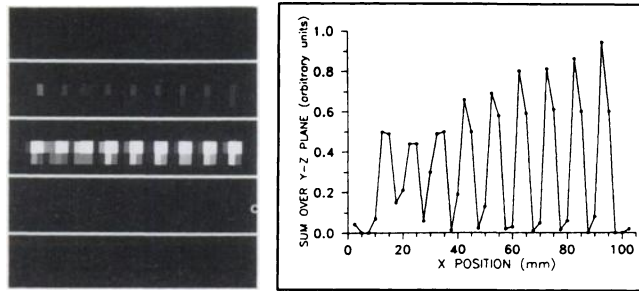
FIGURE 4. (A) Reconstruction of a linear array of point sources. The array was in the axial direction and passed through the center of the aperture hemisphere. The three-dimensional reconstruction is depicted as five longitudinal slices through the array. The point source separation along the array was 10 mm. The reconstruction was performed using an H matrix that was measured in a 5 × 5 × 41 voxel region with a grid spacing of 2.5 mm. (B) Grey level trace along the center of the reconstruction shown in (A).

gion. Structures as small as 5 mm are clearly seen in this figure and one can even discern that the phantom is tilted slightly with respect to the reconstruction planes.

System Sensitivity

We measured the system sensitivity of the brain imaging system in two ways: for a point source and for a distributed source. The point source sensitivity was measured by placing a small ^{99m}Tc source in the center of the FOV of the emulation system. The sensitivity was found to be 9 cps/μCi, indicating that the full brain imaging system would have a system sensitivity of 36 cps/μCi. When the measurement was later repeated on the full prototype system, the measured point-source sensitivity was found to be 32 cps/μCi. The difference between the full system and the emulation system can be accounted for by a slightly different pinhole profile.

The distributed-source sensitivity was measured on the emulation system using a phantom that was 10 cm long by 21.6 cm diameter cylinder. The cylinder was filled with a solution that contained 6520 μCi of activity. This phantom was then placed in the emulation system and imaged

for 100 sec which resulted in a projection data set with 1.38 million counts. Based upon these measurements, the sensitivity of the emulation imaging system was found to be 775 cps per μCi/cc per axial cm. Therefore, the full brain imager was calculated to have a system sensitivity of 3,100 cps per μCi/cc per cm.

To demonstrate the sensitivity of the imaging system, we collected a second data set with conditions similar to those used for Figure 5 but with an exposure of only 10 sec. In this case, the projection data contained 560,000 counts. Figure 6 compares the most representative plane from Figure 5 with the corresponding plane from the three-dimensional image reconstructed from the 10-sec data. Even with this very short exposure, a good image is obtained and the 5-mm features are still easily seen.

System Sensitivity and Multiplexing

Because of the multiplexing that is present in a coded-aperture imaging system, the number of photons that such a system collects is not necessarily a good indicator of the ability of the system to perform a desired imaging task. Each photon collected in a system with multiplexing
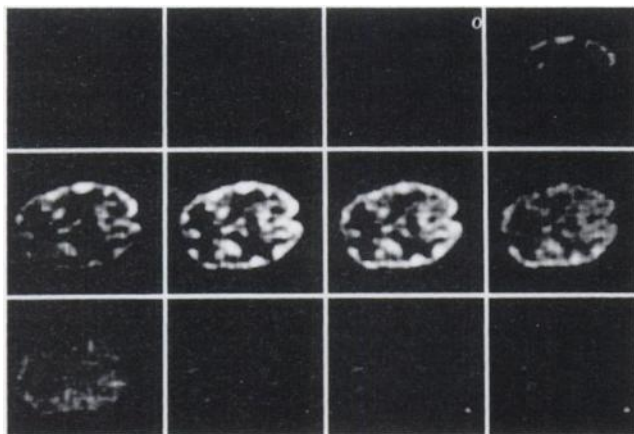

FIGURE 5. Reconstruction of the Hoffman brain phantom. The phantom was oriented parallel to the base of the hemispherical aperture and contained approximately 3 mCi of ^{99m}Tc. Thirty-four million counts were acquired in a 10-min exposure. The reconstruction was performed using an H matrix that was measured with a grid spacing of 10 mm and then interpolated to a grid spacing of 3.3 mm as described in the text.
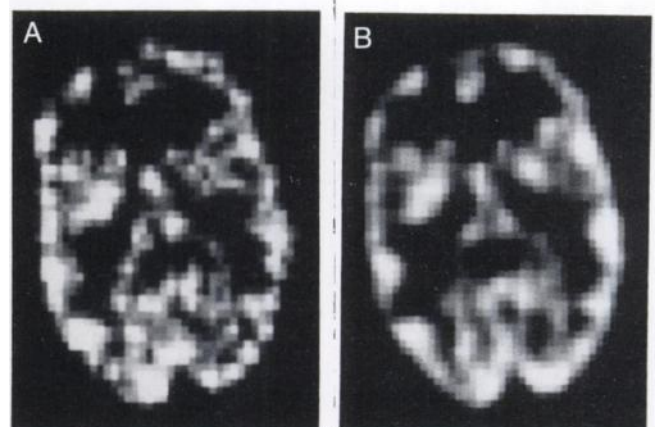

FIGURE 6. (A) Single slice through a three-dimensional reconstruction of the Hoffman brain phantom using a data set identical to that used for Figure 5 except that the exposure time was only 10 sec. (B) Corresponding slice from Figure 5 for comparison.

conveys less information than a photon collected in a system without multiplexing. In order to calculate the magnitude of this effect, we devised a detection task that allowed us to compare the performance of the simulated brain imager with a nonmultiplexing, but otherwise similar, SPECT system. We calculated the ratio between the number of photons required in the multiplexed and non-multiplexed systems to achieve the same level of task performance. This ratio could then be applied to the measured system sensitivity specifications to determine the corresponding effective sensitivity values.

The task that we chose as a means to quantify the effective sensitivity of the brain imager was the detection of a small feature within a simulated phantom. Specifically, we wished to determine the ability of an ideal observer to determine the presence or absence of a 1-cm diameter lesion within the digital brain phantom using just the raw projection data. Such an observer would use a log-likelihood ratio of the form (11):

$$\lambda(g) = \ln[p(g|H_1)] - \ln[p(g|H_0)], \qquad \text{Eq. 2}$$

where g is a vector of projection data measurements, H_1 represents the hypothesis that the signal (lesion) is present, and H_0 represents the hypothesis that the signal is absent (null hypothesis). The appropriate decision rule is to choose H_1 if $\lambda(g) > \lambda_{th}$ and H_0 if $\lambda(g) < \lambda_{th}$, where λ_{th} is the log-likelihood threshold.

The ability to make an accurate decision can be quantified by the signal-to-noise ratio associated with the log-likelihood ratio. This value is known as the detectability and is given by

$$d' = \frac{\langle \lambda|H_1 \rangle - \langle \lambda|H_0 \rangle}{\sigma_\lambda}, \qquad \text{Eq. 3}$$

where $\langle \lambda|H_X \rangle$ denotes the expectation value of the decision variable λ, given that the hypothesis H_X is true, and σ_λ is the standard deviation of the decision variable λ and is assumed to be constant under either hypothesis. A decision task that has a large d' value associated with it is more accurate than a decision task with a smaller associated d' value.

It is straightforward to show that for the case of a data set containing N measurements that include Poisson noise, such as the projection data that we used, and using a Gaussian approximation to that noise, the detectability is given by

$$d' = \left(\sum_{i=1}^{N} \frac{(< g_i|H_1 > - < g_i|H_0 >)^2}{< g_i|H_0 >} \right)^{1/2}. \qquad \text{Eq. 4}$$

We used the simulation techniques described previously to generate two multiplexed projection data sets that were then used in conjunction with Equation 4 to determine the detectability of a small lesion. The config-

uration of the simulated system closely modeled the parameters of the laboratory prototype system. The first set of projection data used a finely sampled version of the digital brain phantom shown in Figure 2A, including the 1-cm lesion shown in the upper left side of the tenth and eleventh slices in the figure. The second projection data set was generated using a similar digital phantom, but without the 1-cm diameter lesion. Both sets of projection data included effects due to an ellipsoidal attenuator and were scaled to reflect the mean number of counts that would be collected when the brain-plus-lesion phantom containing 1 mCi of activity was imaged for 10 min. These multiplexed projection data were then processed according to Equation 4 to yield a lesion detectability value of 5.6.

We then repeated the simulations using the same system geometry, but with no multiplexing. To do this, we modeled a nonphysical system in which there were 100 modular cameras arranged in sets of five modules. All five of the modules within a set occupied the same space but each was associated with only a single pinhole. Therefore, the same projection data were collected as in the multiplexed case, but without any multiplexing. The detectability value in this case was 6.3.

Since d'^2 is proportional to the mean number of counts in the projection data set and the d'^2 value for the multiplexed data was 79% of the d'^2 value for the nonmultiplexed case, then the data collected by a coded aperture similar to the one used by the brain imager provided information about the lesion equivalent to a nonmultiplexed data set with 21% fewer counts. By this measurement, the effective sensitivity values of the brain imager are 79% of the measured sensitivity values.

DISCUSSION

Although the results from the laboratory prototype have demonstrated that the current system configuration and algorithms produce good three-dimensional reconstructions, further theoretical and experimental work will be required to make necessary improvements to the system. For example, we expect that the final aperture will contain baffles and/or directionally sensitive pinholes to minimize the effect of out-of-field activity from the lungs and other nontarget regions of high isotope concentration. Also, the number and placement of the pinholes will likely be modified and additional modular cameras will be added to improve the angular sampling within the FOV.

The method that we use to separate the system matrix into two components, and thereby greatly reduce the calibration time and data storage requirements, requires some additional refinement. Although the R matrix is easier to interpolate than the H matrix, it is still difficult to properly interpolate the R matrix in all cases. At the time of these experiments, we used a relatively simple, but error-prone, interpolation technique. A more sophis-

ticated technique is currently being developed that should alleviate the problems due to erroneous interpolation once it is implemented.

The current method of separating the H matrix operates under the assumption that the pinhole projection profile, or blur, contained in the B matrix depends on only the centroid location and not on the point source location. However, due to magnification effects, this assumption is not strictly true. We have formulated, but not yet implemented, a new separation algorithm that maintains information about the individual pinhole-projection sizes while still allowing us to greatly reduce the size of the system calibration data that must be stored.

Finally, the key assumption that allows the size of the blur matrix to be drastically reduced is that the pinhole projection profile is relatively compact. Under this assumption, the values of only a small number of detector pixels need to be stored for each blur. However, in order to include scatter correction in the reconstruction algorithm, the size of the blur region, and hence the size of the B matrix, may have to be greatly increased to adequately model the effect of the scattered photons.

CONCLUSION

This paper describes a new class of three-dimensional SPECT systems for imaging the human brain. These systems consist of a hemispherical multiple-pinhole coded aperture and a hemispherical detector surface made up of an array of modular gamma cameras. Such imagers are capable of collecting all of the data necessary to generate three-dimensional reconstructions without motion of either the aperture or the detectors. A related part of this research has been devoted to the development of an efficient method to measure, store and use the actual system response function during the reconstruction process.

We have demonstrated the performance of the three-dimensional brain imager with reconstructions produced by both simulated and real systems and by performance specifications measured on two laboratory versions of the imaging system. The results presented in this paper are

encouraging and seem to indicate the viability of this method of SPECT imaging. However, we believe that the imaging system configuration and algorithms used to produce the results in this paper can be improved. Therefore, further research will be required to determine the ultimate capabilities of this class of imaging system.

REFERENCES

1. Aarsvold JN, Barrett HH, Chen J, et al. Modular scintillation cameras: a progress report. SPIE Medical Imaging II: Image Formation, Detection, Processing, and Interpretation 1988;914:319–325.
2. Milster TD, Selberg LA, Barrett HH, et al. A modular scintillation camera for use in nuclear medicine. IEEE Trans Nucl Sci 1984;NS-31: 578–580.
3. Milster TD, Selberg LA, Barrett HH, Landesman AL, Seacat III RH. Digital position estimation for the modular scintillation camera. IEEE Trans Nucl Sci 1985;NS-32:748–752.
4. Milster TD, Aarsvold JN, Barrett HH, et al. A full-field modular gamma camera. J Nucl Med 1990;31:632–639.
5. Roney TJ, Aarsvold JN, Barrett HH, et al. Modular scintillation cameras: status and applications [Abstract]. J Nucl Med 1988;29:760.
6. Roney TJ. Coded-aperture transaxial tomography using modular gamma cameras. PhD dissertation, University of Arizona, Tucson, 1989.
7. Rogers SC. Efficient sampling for dynamic single-photon emission computed tomographic imaging. MS thesis, University of Arizona, Tucson 1990.
8. Rowe RK, Barrett HH, Patton DD. A design study for a stationary 3D SPECT brain imaging system [Abstract]. J Nucl Med 1990;31:769.
9. Rowe RK, Aarsvold JN, Barrett HH, et al. The design and implementation of modular SPECT imaging systems, In: Todd-Pokropek AE, Viergever MA, eds. Medical images: formation, handling, and evaluation. NATO-ASI Series, Heidelberg: Springer-Verlag, 1992.
10. Rowe RK. A system for three-dimensional SPECT without motion. Ph.D. dissertation, University of Arizona, Tucson 1991.
11. Van Trees HL. Detection, estimation, and modulation theory: part I. New York: John Wiley & Sons, 1968.